Direct evidence of high pore pressure at the toe of the Nankai accretionary prism

J. Pwavodi[1], M.-L. Doan [1]and the IODP Expedition 358 Science Party

[1]Univ. Grenoble Alpes, Univ. Savoie Mont Blanc, CNRS, IRD, UGE, ISTerre, 38000 Grenoble, France

Key Points:

- Drilling and geophysical data were used to get continuous hydraulic properties along Hole C0024A at the toe of the Nankai accretionary prism.
- Overpressure rises from few hundred meters above the décollement, in hemipelagites, to reach 62% above hydrostatic pressure at the plate boundary.
- The damage zone is more developed in the footwall of the décollement, which itself is impermeable across the fault core.

Corresponding author: Joshua Pwavodi, joshua.pwavodi@univ-grenoble-alpes.fr

Abstract

The Nankai Trough is a locus of slow slip, low frequency earthquakes and $M_w > 8$ classical earthquakes. It is assumed that high pore pressure contributes substantially to earthquake dynamics. Hence, a full understanding of the hydraulic regime of the Nankai accretionary prism is needed to understand this diversity of behaviors. We contribute to this understanding by innovatively integrating the drilling and logging data of the NanTroSEIZE project. We focus on the toe of the accretionary prism by studying data from Hole C0024A drilled and intersected the décollement at 813 mbsf about 3km away from the trench.

Down Hole Annular Pressure was monitored during drilling. We perform a careful quantitative reanalysis of its variation and show localized fluid exchange between the formation and the borehole (excess of 0.05 m^3/s), especially in the damage zones at the footwall of the décollement.

Pore pressure was estimated using Eaton's method on both drilling and sonic velocity data. The formation fluids are getting significantly over-pressurized only a few hundred meters from the toe of the accretionary prism near the décollement with excess pore-pressure ($P^* \approx 0.04$–4.79 MPa) and lithostatic load ($\lambda \approx 0.88 - 0.96$ & $\lambda^* \approx 0.1 - 0.62$) contributing to maximum 62% of the overburden stress.

The hydraulic profile suggests that the plate boundary acts as a barrier inhibiting upward fluid convection, as well as a lateral channel along the damage zone, favouring high pore pressure at the footwall. Such high pressure at the toe of the subsection zone makes high pressure probable further down in the locus of tremors and slow slip events.

Plain Language Summary

We combine both drilling and logging data to get a high-resolution quantitative profile of hydraulic properties along hole C0024A, which intersected the plate boundary at the frontal thrust of the Nankai subduction. This fine characterisation helps understanding the process controlling the pore pressure buildup and the fluid circulation that affect the mechanical behavior of this active fault zone.

1 Introduction

Tectonic deformation and earthquake cycle are substantially driven by high pressure fluids trapped at depth (Miller, 2013). In subduction zones, these fluids are released by mineral dehydration and sediment compaction, affecting the effective stress on faults (Saffer & Tobin, 2011). Elevated pore pressure has also been considered as a key factor governing a host of recently discovered fault slip behaviours along subduction thrusts, including very low-frequency earthquakes (VLFE), episodic tremor and slip (ETS), and slow slip events (SSE) (Audet et al., 2009; Kodaira et al., 2004). It has also been shown that the SSE were synchronous with recorded transient pore pressure pulses (Araki et al., 2017), suggesting that hydrogeologic properties were key to understanding the fault mechanics of the subduction zone.

However, getting an estimate of pore pressure is difficult (Saffer & Tobin, 2011). A first method is the combination of laboratory compaction experiments coupled with numerical simulation of the building of the accretionary prism calibrated with the hydro-mechanical properties derived in the laboratory from cores. However, this approach is limited by strong assumptions on the representativeness of the core samples on which the compaction experiments were done. In addition, the numerical modelling of the building of the whole prism is large scale, ignoring the complexity of the accretionary prism build-up. A second method, based on geophysical imaging of the seismic velocity, has coarse resolution because of the low frequency data of deep seismic surveys and because strong calibration is needed to convert seismic anomalies into hydrogeologic quantities. Finally, a third method relies on borehole observatories, which provide an accurate time series of pore pressures at a single location only. Therefore, they don't document the spatial variability along the entire borehole. The use of industry tools to determine hydrological properties (eg, NMR logging tools and MDT formation tester (Boutt et al., 2012; Thu et al., 2012; Saffer et al., 2013) and has limited use in academic studies due to its large cost.

The low permeable underthrust sediments of the décollement in Nankai trough are characterised by vertical dewatering, which is a precursor for flow patterns and pore pressures higher than hydrostatic pressures(E. Screaton & Ge, 1997; E. J. Screaton & Saffer, 2005; Gamage & Screaton, 2006; E. Screaton, 2006). The predicted pore pressure is in excess of 5-32 MPa values above the hydrostatics, also with systematic increasing values landwards of the trench (Tobin & Saffer, 2009). In an attempt to further show the evidence of high

pore pressure in Nankai Trough, J. C. Moore et al. (2013) noticed that the acquired drilling DownHole Annular Pressure (DHAP) data varies consistently with anomalies of the seismic profiles done on the Nankai trench, but he did not quantitatively interpret these data.

Even though Nankai Trough has been the focus of a major scientific project, there is no definitive quantification of the elevated pore pressure within the overlying décollement within the accretionary prism. Here, in this study, we combine drilling engineering methods with geophysical approaches. Especially, we used two independent methods to quantitatively estimate the hydrogeological properties of the Nankai accretionary prism:

a. DHAP (mud pressure during drilling operation) modelling for fluid fluxes between borehole and formation
b. Pore pressure estimation using Eaton's method (using either drilling data or sonic travel time equations)

The results from these methods were compared to get self-consistent view of the hydraulic properties along the borehole with definite interpretation around the décollement zone. The originality of our methodology used a large span of both logging data (depth-based) and drilling data (time-based). It's advantageous working with both time evolution and depth because of its ability to relocate each hydraulic anomaly back to a geological framework.

1.1 Geological setting

The Nankai Trough is formed by the subduction of the Philippine Sea Plate to the northwest underneath the Eurasian Plate with a development rate of 4.8mm/yr to 12.8 mm/yr (Sella et al., 2002). It is an area of high seismic hazard as exemplified by M8+ 1944 Tonankai 1944 earthquake and the 1946 Nankaido earthquake (Ando, 1975; Hori et al., 2004) shown in Fig. 1a. It has also been identified as a locus of slow slip events (SSE) and very low frequency earthquakes (VFLE) (Araki et al., 2017) with identified predominant frequency of 0.1 Hz near the trench axis of the Nankai Trough (Obara & Ito, 2005). The primary depositional sediments are trench wedge facies (Spinelli & Wang, 2008), which are largely deformed, making Nankai a site of choice for studying accretionary prisms.

The Nankai subduction zone has been the focus of the Nankai Trough Seismogenic Zone Experiment (NanTroSEIZE) project, which features 13 IODP expeditions. As part of

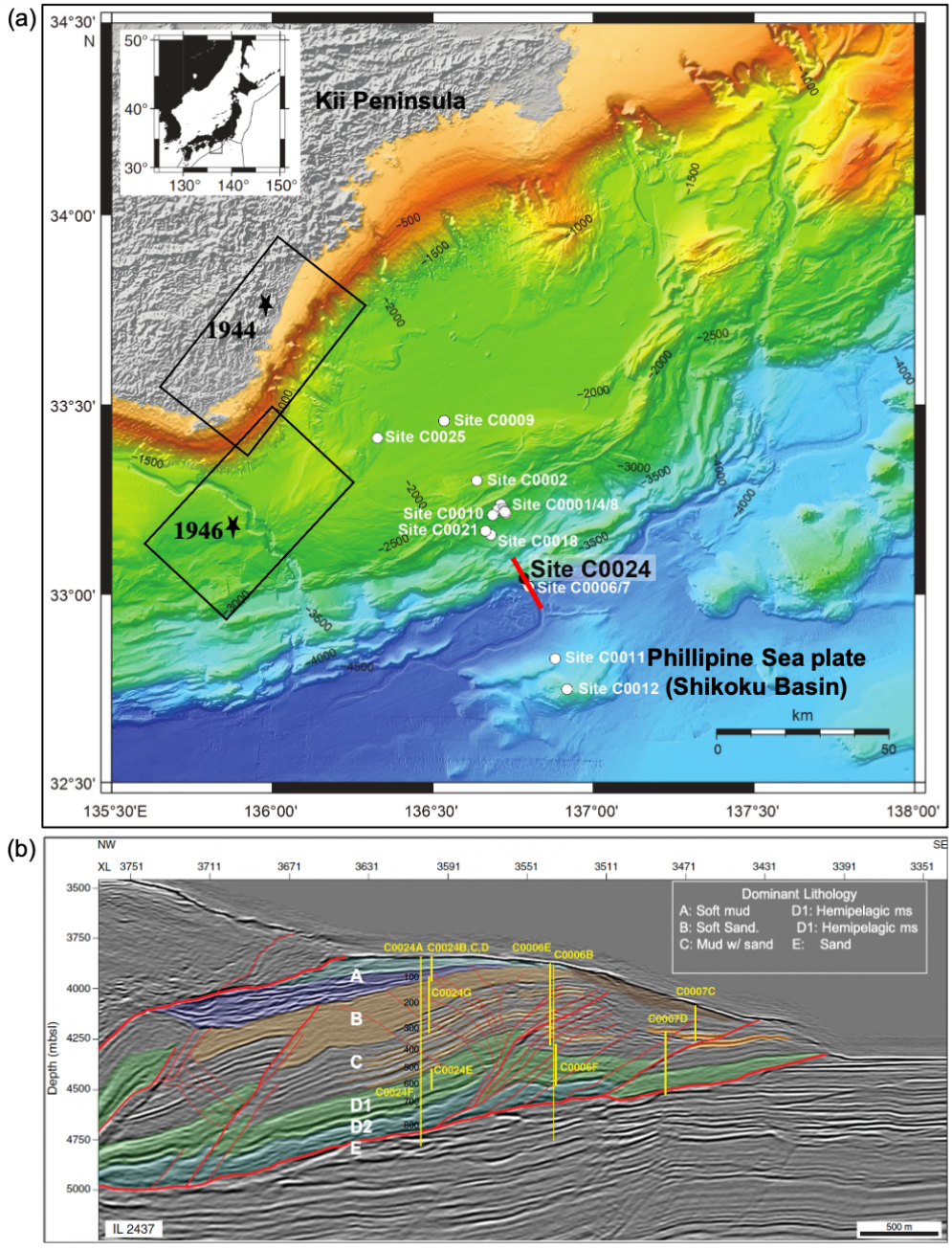

Figure 1. (a) Map of the Nankai subduction zone offshore Japan. The NanTroSEIZE transect is indicated with a black thin line. Site C0024 is represented with a black solid circle while the others holes are represented with white hollow circles. The black rectangles show the location of the two large magnitude earthquakes of 1944 and 1946. (b) Seismic cross section along the red line at the toe of the accretionary prism, with drilled sites C0024, C0006 and C0007(Modified from Tobin et al. (2020)).

Expedition 358, the last stage of the NanTroSEIZE project, hole C0024A was drilled to a depth of 871 mbsf with the objective to investigate the frontal thrust of the region (Tobin et al., 2020). Site C0024 is located a few kilometers northwest of site C0006 in the frontal anticline overlying the frontal thrust (Fig. 1a). The hole C0024A is the deepest drilled hole in the site. This logging while drilling (LWD) drilled hole penetrated the frontal thrust, which was interpreted as a complex zone of fault strands and imbrication of thrust slices at 813 mbsf. Cores were obtained in four other holes, but at shallower intervals as their drilling was abandoned because of deteriorating borehole conditions at deeper levels (Tobin et al., 2020). This site is stratigraphically (Fig. 2a) divided into 3 different logging units (further divided into 6 subunits) with varying thickness and dipping angles. (a) Accretionary trench wedge facies (Unit 1: Subunit 1a, Subunit 1b, Subunit 1c) (b) Shikoku basin hemipelagic-pyroclastic facies (Unit 2: Subunit 2a, Subunit 2b) (c) Unit 3.

2 Methods

The data type used in this work needs relocating hydraulic anomalies back to its real geological spatial framework. The LWD tools provide a time series of drill bit location and data from the geophysical sensors. These data are usually converted to depth-based data by the logging operator, but we keep processing them first as time-based. On Fig. 2 both logging and drilling data are manually depth-converted by computing the first time a given depth is reached and extracting the relevant logging and drilling data at that time.

A typical interesting drilling data used is the DHAP (Fig. 2i), which is recorded 7.5 meters above the drill bit for well C0024A. It's considered as drilling data as it provides mud pressure, not formation pressure. Hence, it is sensitive to changes in drilling operation and needs to be properly modeled to retrieve information about the fluid fluxes between the hole and the formation (Amiri & Doan, 2019). A systematic workflow was used for the DHAP modelling and pore pressure estimation. For ease of reference, a list of symbols and notations used in this paper are given in Table 1.

2.1 DownHole Annular Pressure (DHAP) modelling

Mud pressure is a key factor for maintaining wellbore stability. The DHAP data can be composed of two principal components (static and dynamic pressures), each of which is affected by a variety of parameters, including mud density, mud circulation, direct intake

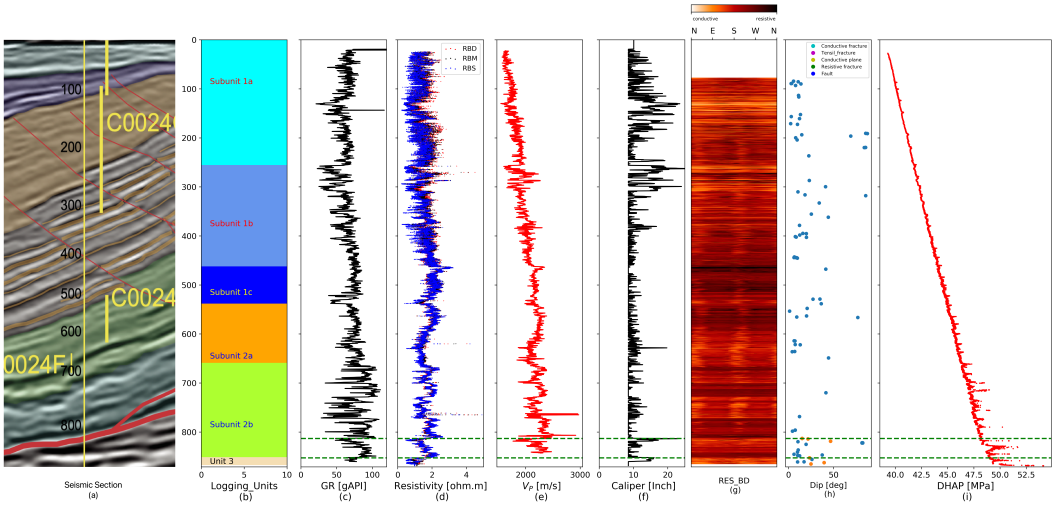

Figure 2. Summary the geophysical data of Hole C0024A. The plate boundary, also called the décollement, has 2 strands highlighted in green at the depths of 813 and 852 mbsf. (a) Focus of the seismic cross-section of Fig. 1b at the location of C00024a. (b) Logging units identified onboard by the science party from logging data (Tobin et al., 2020) (c) Natural gamma-ray log (GR, in API units) (d) Electrical resistivity log (with shallow, medium and deep depths of investigation) in $\Omega \cdot$ m (e) Sonic slowness (δt, in μs/ft). (f) Borehole diameter (caliper) derived from electrical data (g) Electrical borehole image from deep resistivity. Breakouts are visible. (h) Picking of fractures and faults from the borehole image done by the science party onboard (Tobin et al., 2020). (i) Drilling mud pressure (DHAP). We display only the data corresponding to the the first time any drilled depth was reached. (see methods for description of the processing).

Table 1. List of symbols and notations

Symbol or acronym	Meaning
BHA	BottomHole Assembly (equipment at the base of the drill string)
d_b	Diameter of the borehole (= caliper)
d_p	Diameter of the drill string (pipe or BHA, depending on depth considered)
DHAP	DownHole Annular Pressure
ECD	Equivalent Circulating Density
ROP	Rate of Penetration
RPM	Rotation Per Minute of the drill string
HL	Function relating hydraulic loss to flow rate (Eq. 8)
Q_{out}	Total flow rate flowing upwards in the annulus above DHAP sensor (Fig.. 4)
Q_{pump}	Flow rate of clean mud pumped into the borehole
Q_f	Additional flow from the formation.
P_{sea}	Seawater Pressure at the seafloor or mudline (Fig. 4)
ϕ	Porosity of the rock formation
MW	Mud weight
mbsf	Meters below seafloor
r_i	Radius of influence of a pressure disturbance within the borehole
$\bar{v}$	Average mud velocity within the borehole annulus
Z	True Vertical Depth (TVD)
ρ_{eff}	Effective density of the mud, cuttings included
ρ_{MW}	"Mud Weight", i.e. density of the clean mud, free of cuttings
ρ_g	Density of the rock matrix (=grain density)
ρ_r	Density of the rock formation
ρ_w	Density of the fluid filling the pores of the rock , assumed to be seawater
$\rho_{dyn+fluid\ flow}$	Pressure loss due to dynamic effects and fluid flow
μ	Dynamic viscosity of the mud

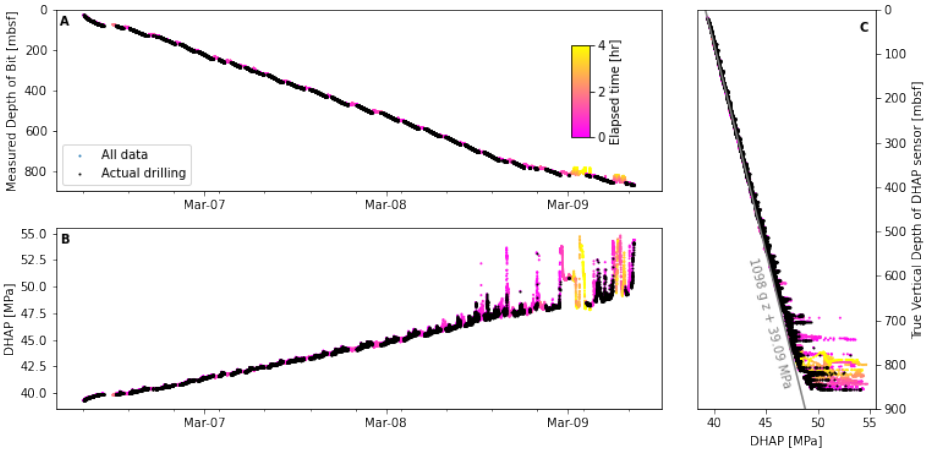

Figure 3. Time series of drilling data, especially bit depth (part A) and DHAP (part B), color-coded by the duration between the DHAP measurement at each depth since drilling at this depth. DHAP and bit depth tend to increase with time. We restrict our analysis to the DHAP data when each depth was first reached by the drill bit (black data). DHAP increases with the true vertical depth of the DHAP sensor (part C), with a linear baseline (in gray) corresponding to an equivalent mud density of 1098 kg/m^3.

from the formation into the borehole annulus, pipe velocity (swab, surge, and drill pipe rotation), and pressure loss. To simulate the DHAP successfully, we examined the following contributions to the DHAP:

a. Pressure increases with depth due to hydrostatic pressure. The effective mud weight (ρ_{eff}) will take into account both the density of the clean mud (ρ_{MW}) as measured in the onboard mud tank and the weight of cuttings, which are rock fragments formed during drilling and carried out of the hole by the mud.
b. Dynamic hydraulic overpressure induced during pumping by fluid circulation.
c. Any anomalies from the previous modeling are attributable to flow (Q_f) between the well and the surrounding rock formation.

We assume that swabs and surges are negligible because the interpretation of DHAP is restricted to the dataset corresponding to the times corresponding to actual drilling. This modelling process will involve the three following contributions to DHAP stated above.

2.1.1 Contribution of cuttings

Drilling mud is returned to the surface in either continental drilling or riser oceanic drilling operations. The weight of the returned mud surpasses the weight of the mud that was first injected because the mud conveys cuttings, which are rock fragments formed during the drilling operation and are heavier than the original mud. However, because hole C0024A was drilled with a riserless system, we do not have any direct information about the contribution of the cuttings to the drilling mud because it was lost to the seafloor.

Fig.3 shows that when plotting DHAP vs depth, it tends to align along a baseline with a slope of 10.07 kPa/m equating to an equivalent density of 1098 kg/m3. In this case, the clean mud weight is the greatest possible value (as cuttings and dynamic hydraulic loss also contribute). This is in conflict with the official mud reports, which have contradicting numbers ranging (1150 and 1350 kg/m3). As a result, we will investigate a broad range of probable values for the clean mud weight (ρ_{MW}).

The mass balance principle is used to estimate the effective mud density (which is the combination of clean mud density and cutting density). For the sake of this calculation, the following assumptions were made:

a. Within the borehole is a homogeneous mud with an effective density (ρ_{eff}) that is assumed to be independent of temperature, pressure, and therefore depth.
b. The amount of mud that returns to the seafloor is equal to the amount of mud that leaves the pumps (i.e., no mud loss , neither storage within the pipes and annulus). For the sake of this estimation, the flow rate (Qf) between the formation and the hole is considered to be minimal in comparison to the pumping rate ($Qpump$).

Mass balance is made on the Eulerian volume system shown in Fig. 4. This volume encompasses the current borehole volume (V_{bor}) and the volume $dV = ROP\, dt\, \pi\, \frac{d_b^2}{4}$ of rock to be drilled between initial drilling time (t_0) and total drilled time ($t_0 + dt$). The latter volume is controlled by the Rate of Penetration (ROP), a standard drilling data, and the borehole diameter (d_b), which is constrained between the nominal bit size and the borehole caliper measured at the time of the passing of the electromagnetic tool, typically several tens of minutes after drilling (Fig. 3). We used the caliper values in our calculation to get the upper estimate of the contribution of the cuttings.

The initial mass within this volume is $M_0 = M(t_0) = \rho_{\text{eff}}\, V_{bor} + \rho_r\, dV$ and after drilling, it becomes $M(t_0 + dt) = M_0 + dM = \rho_{\text{eff}}\ (V_{bor} + dV)$. The mass change ($dM$) is accommodated by the mass increase due to clean mud coming pumped into the borehole ($\rho_{MW} Q_{pump} dt$) and by the mass loss due to the outflow of cutting-loaded mud at the mudline ($-\rho_{\text{eff}} Q_{out} dt$). As flow to and from the formation is considered negligible, $Q_{out} \simeq Q_{pump}$ and the mass balance equation provides an estimate of the effective density (ρ_{eff}) of the mud loaded with cuttings :

$$\rho_{\text{eff}} = \frac{\rho_{MW} Q_{pump} + \rho_r\, ROP\, \pi\, \frac{d_b^2}{4}}{ROP\, \pi\, \frac{d_b^2}{4} + Q_{pump}} \tag{1}$$

Given that the cores could not be recovered for most of the borehole, the bulk density of the formation was estimated as $\rho_r = \rho_g\,(1-\phi) + \rho_w \phi$, where ρ_g is the grain density determined from the cored section, ρ_w is the density of the salted water filling the pores of the rock (assumed to be seawater so that $\rho_w = 1028\,\text{kg/m}^3$) and ϕ is the rock porosity, as estimated onboard from resistivity logs (Tobin et al., 2020).

2.1.2 Contribution of dynamic hydraulic losses

Due to the viscosity of the mud, increased mud pressure at the bottom of the hole is required to allow the mud to flow back to the sea via the borehole annulus. Hydraulic resistance will cause a difference in pressure between the annular pressure at the DHAP sensor position and the seafloor, which depends on the flow circulating through the annulus.

As a first approximation, it is assumed that any flow Qf between the formation and the well occurs only below the DHAP sensor, and thus that the hydraulic loss along the drill string between the DHAP sensor and the surface can be calculated using the known pumping rate Q_{pump}, since $Q_{out} = Q_f + Q_{pump}$. Drilling mud forms a "mud-cake" on the borehole wall, which thickens and becomes impermeable with time and distance from the drill bit, (Dewan & Chenevert, 2001).

Hydraulic resistance is a function of the hydrodynamic regime in which it exists. The average velocity, effective density, hydraulic diameter, and viscosity are the critical factors used to get the Reynolds number (Re) (equation 2). If the $Re \ll 2000$ and $Re \gg 4000$ are used, the hydraulic regime will be deemed laminar and turbulent, respectively. The dimensionless Reynolds number is a critical quantity that influences the choice of frictional pressure loss equations.

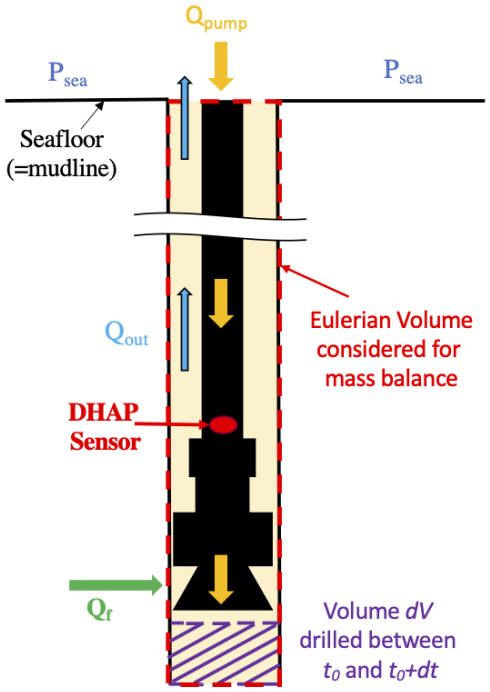

Figure 4. Schematics of the Eulerian system on which mass balance was conducted (delimited by red dashed lines). The volume drilled between t_0 and t_0+dt is shown with purple stripes. Arrows show also the fluid flows considered. Both the pumping flow Q_{pump} and the flow coming from the formation Q_f (positive in case of influx to the borehole, negative in case of outflux) contribute to the flow returning to surface Q_{out}. The fluid flow into the well is assumed to come from a section between the DHAP sensor and the drill bit. Above, an impermeable mud cake is supposed to be fully developed.

$$Re = \frac{\rho_{\text{eff}}\,\bar{v}\,d_e}{\mu} \tag{2}$$

Where Re is the Reynolds number which is dimensionless, ρ_{eff} is the effective density in kg/m^3 (Eq. 1), μ is the dynamic (or absolute) viscosity of fluid in Pa $\cdot$ s, $\bar{v}$ the annular average velocity and d_e the hydraulic diameter, which is a function of the diameter of borehole, d_b and the outside diameter of the pipe (m), d_p (Bourgoyne et al., 1986) :

$$d_e = \sqrt{d_b^2 + d_p^2 - \frac{d_b^2 - d_p^2}{\ln\left(\frac{d_b}{d_p}\right)}} \tag{3}$$

This average flow velocity $\bar{v}$ is estimated through the mass balance equation, providing a direct relationship with the flow rate and an inverse relationship with the surface area of the drilling system (BHA, pipe and borehole diameter) :

$$\bar{v} \;=\; \frac{4\,Q_{out}}{\pi\left({d_b}^2 - \;{d_p}^2\right)} \tag{4}$$

Where Q_{out} is the upwards flow rate in m^3/s.

During drilling, flow rates always exceed 0.02 m/s. The result indicates a turbulent flow regime in the entire column of the borehole annulus with Reynolds number above $Re \gg 50000$. For a turbulent regime, the hydraulic flow through an interval section of length dz can be determined through the Fanning equation (Bourgoyne et al., 1986) (equation 5) :

$$\frac{dp_f}{dz} = \frac{2f\rho_{\text{eff}}\bar{v}^2}{d_e} \tag{5}$$

where for an annulus between two cylinders of inner and outer diameters, respectively, d_p and d_b, can be expressed as and f is the Fanning friction coefficient (equation 6). Blasius (1913) shows that the Fanning coefficient is related to the Reynolds number in a simple way (Bourgoyne et al., 1986), provided we ignore the roughness of the pipe walls.

$$f = \frac{B}{Re^{1/4}} \tag{6}$$

where experimentally, $B = 0.0791$.

Combining equations 5 and 6, we get the appropriate pressure loss equation for a Newtonian fluid turbulence model based on the Fanning equations (Bourgoyne et al., 1986) expressing the gradient of frictional pressure drop dp along a section of borehole (an annulus) of length dz stated in equation 7.

$$dp_f \;=\; 2\,B\,\frac{\rho_{\text{eff}}^{3/4}\bar{v}^{7/4}\mu^{1/4}}{d_e(z)^{5/4}}dz \tag{7}$$

Where; dp_f is the pressure loss (in Pa), ρ_{eff} is the effective mud density (in kg/m3), as computed previously, dz the length of the annulus (m). In this equation, fluid is assumed to be incompressible and the flow from the formation does not build up pressure, because it just escapes to the surface through the well annulus. Equation 7 is then combined with equations 4 and 3 and integrated between the seafloor and the current depth z_{DHAP} of the DHAP sensor, so that the hydrodynamic contribution would be computed as :

$$\Delta p(z_{DHAP}) = \frac{4^{9/4}\, B\, Q_{out}^{7/4}}{\pi^{7/4}} F\left(z_{DHAP}\right) = HL\left(Q_{out}\right) \tag{8}$$

with all depth-dependent terms bundled in the term $F(z_{DHAP})$. For each depth considered, we took into account the actual borehole diameter and the actual configuration of the drill string.

$$F\left(z_{DHAP}\right) = \int_0^{z_{DHAP}} \frac{\rho_{\text{eff}}(z)^{3/4}\, \mu(z)^{1/4}}{\left(d_b\left(z\right)^2 + d_p\left(z\right)^2 - \frac{d_b(z)^2 - d_p(z)^2}{\ln\left(\frac{d_b(z)}{d_p(z)}\right)}\right)^{5/8} \left(d_b\left(z\right)^2 \; - \; d_p\left(z\right)^2\right)^{7/4}} dz \tag{9}$$

Viscosity is a key parameter in the above equations. A service company onboard made systematic rheological measurements on the mud prepared for drilling. This tank mud is thixotropic with viscosity varying between $2 \times 10^{-3}\,\text{Pa}\cdot\text{s}$ and $52 \times 10^{-3}\,\text{Pa}\cdot\text{s}$ for viscosity rotation rate between 1 and 600 rpm. However, there is an inconsistency between the official injected mud weight and the effective mud weight determined from actual DHAP data (Fig. 3). Because of this uncertainty on the actual composition of the borehole fluid, we first forward-estimated the hydrodynamic contribution assuming the fluid was purely Newtonian and testing wide range of viscosity, with the viscosity of water ($10^{-3}\,\text{Pa}\cdot\text{s}$) as an underestimate and the maximum viscosity for the tank mud ($52 \times 10^{-3}\,\text{Pa}\cdot\text{s}$) as an overestimate. To simplify the inversion, we also assume that the mud viscosity and density is uniform within the borehole, as a reasonable assumption, as the mud is circulating during this drilling, uniforming the mud properties along the hole. We keep the value of viscosity so that we can fit at best the baseline of DHAP data (Fig. 3).

2.1.3 Estimation of the flow between formation and borehole

Any anomaly not captured by the previous DHAP modelling steps above is attributed to the fluid exchange between the well and the surrounding rock formation. Hence, it is convenient to use equation 8 to convert the unexplained DHAP anomaly into an anomaly

in the vertical upward flow. Hence, the fluid flow Q_f between fluid and formation is given as

$$Q_f = Q_{out} - Q_{pump} \tag{10}$$

$$= HL^{-1}\left(DHAP - \rho_{\text{eff}} gz - P_{sea}\right) - Q_{pump} \tag{11}$$

where HL is the hydraulic loss function introduced in equation 8, whose fluid parameters were adjusted to fit the baseline of the DHAP profile (Fig. 3).

The intensity of this incoming flow is depending on at least two factors : (1) the permeability of the rock formation and (2) the pressure difference between the formation and the borehole. Hence, an estimate of the pore pressure is necessary to analyse quantitatively the inflow data.

2.2 Pore pressure estimation

Pore pressure conditions are controlled by the permeability and fluid retention capacity of the rock formation, as well as its loading history. Most studies used to predict over-pressure in subduction zones are carried out using indirect identification methods including traditional theoretical analysis and numerical simulation. However, this study uses Eaton empirical method (Eaton, 1972, 1975) which has been used widely to predict the pore pressure gradient by comparing *in situ* lithology physical properties with overburden pressure gradient and the normal compaction trend line (NCTL) in shale.

During sedimentation and diagenesis, porosity decreases due to the increasing overburden associated with burial and compaction. The NCTL represents the expected evolution in case of a simple drained diagenesis process, in which the pressure keeps hydrostatic (Terzaghi et al., 1968). Higher fluid pressure generation is associated with other tectonic or slope evolution events that are common in subduction prisms. Hence, the physical and mechanical properties tend to deviate from the NCTL line. Eaton theory has been applied in drilling theory to derive pore pressure prediction from drilling data (Jorden & Shirley, 1966) or sonic velocities (Eaton, 1975).

Overburden gradient (OBG) is the quantity $\rho_r(z)\, g$, where $\rho_r(z)$ is the bulk density of the rock and g is the gravity acceleration. Over-pressured zones tend to show an abnormal deviation from the normal trend of these parameters, which depicts the variability in lithology, fluid content, and structure. This equation is valid if the correct NCTL can be

determined for all depths of interest; otherwise, the pore pressure will be overestimated or underestimated, therefore increasing the drilling risk. Pore pressure can be hydrostatic at shallower zones but can rapidly increase with depth depicting hydraulically isolated formations with different properties compared to the ones above it. The empirical methods used in this manuscript are based on (1) *d*-exponent method from drilling data and (2) sonic transit time method.

2.2.1 d-exponent method from drilling data

The *d*-exponent (d_x) method is a quantity used in the drilling industry to delineate the empirical relationship between rock strength, bit size, and formation drillability (Bingham, 1965). When the lithology is constant and no other variables change, the penetration rate decreases as compaction increases. If the penetration rate increases in a uniform argillaceous sequence, however, it indicates undercompaction.

Therefore, this method accounts for the normalisation of the ROP for quantifying overpressure, since ROP increases rapidly in overpressured zones associated with undercompacted shaly sand. In a typical Eaton mode, ROP vs depth should follow an exponential decay law with depth. Higher pore pressure facilitates rock failure and ROP increases rapidly. Thus, in the actual equation, it accounts for drillability, since ROP depends on the weight on bit (WOB) and the rotation rate of the drillstring (RPM). However, it is noted that under variable drilling conditions, a recognizable relationship between differential pressure and *d*-exponent exists by Jorden and Shirley (1966).

$$d_x = \frac{\log\left(\frac{\mathrm{ROP}}{60\,\mathrm{RPM}}\right)}{\log\left(\frac{12\,\mathrm{WOB}}{10^6\ d_b}\right)} \tag{12}$$

Where: d_x is the *d*-exponent (dimensionless), ROP (ft/h), RPM is the rotary speed (rpm), WOB is downhole weight on bit (lbf), d_b is the bit diameter (in). The *d*-exponent increases with increasing depth for a lithology, with constant bit type, mud overbalance and increasing compaction. Trend deviations of *d*-exponent can be experienced when drilling through overpressured zones and by varying mud density due to overbalance. To remove the effect of mud density changes for *d*-exponent to respond predictably to pore pressure gradient, Rehm and McClendon (1971) proposed a correction to *d*-exponent called d_{xc} (equation 12).

$$d_{xc} = d_x \left(\frac{\rho_{MW}}{\text{ECD}}\right) \tag{13}$$

Where ρ_{MW} is the clean mud weight (g/cm^3), and ECD is the Effective Circulation Density. ECD was recomputed using equation 14 (adapted for a riserless hole) because it gives an intuitive way to interpret the fluid pressure (DHAP), that steadily increases with depth (Fig. 3). The estimated ECD is a key input for the Eaton d-exponent computation for pore pressure calculations (equation. 13).

$$ECD = \frac{DHAP - P_{sea}}{g\ Z} \tag{14}$$

Where P_{sea} is the pressure at the mudline (seafloor), Z is the True vertical Depth (TVD) in meter below seafloor (mbsf) and g is acceleration due to gravity (9.81 m/s^2).

$$HPG = \frac{(P_{sea} + \rho_w\, g\, Z) - P_{sea}}{Z} = \rho_w\, g \tag{15}$$

$$OBG = \frac{\left(P_{sea} + \int_0^Z \rho_b(Z)\, g\, dZ\right) - P_{sea}}{Z} = \frac{\int_0^Z \rho_b(Z)\, dZ}{Z}\, g \tag{16}$$

Jorden and Shirley (1966) proposed that the Pore Pressure Gradient (PPG) could be determined from the d-exponent and substituting the overburden gradient (OBG)(equation 16) and the hydrostatic pressure gradient (HPG) (equation. 15) into equation 17. The parameter d_n (normal trend) of d_{xc} coefficient (NCT) within the shale can be ascertained with equation 18. The NCTL was evaluated considering the sediment compaction trend over the main logging units identified onboard (Fig. 1a): (1) slope basin facies (<112 mbsf), (2) accretionary trench-wedge sediments (3) hemipelagic-pyroclastic facies (Shikoku Basin) (>555 mbsf). We made a critical assumption that the shallow depth sediments are normally pressured, so we made a very reasonable linear fit to the surface:

$$PPG = OBG - (OBG - HPG)\left(\frac{d_{xc}}{d_n}\right)^n \tag{17}$$

$$d_n = d_0 + d\, Z \tag{18}$$

$$PPG = \frac{P_f - P_{sea}}{Z} \Rightarrow P_f = P_{sea} + PPG \times Z \tag{19}$$

Where d_n is the normal trend of d_{xc} coefficient (NCT) and n is an empirical exponent, d_0 is the shale d-exponent value at the mudline, d is calibration parameter, Z is the true vertical depth below mudline (in mbsf). The value of exponent n in equation 18 varies between 0.6 and 1.5, with normally $n = 1.2$ (Zhang & Yin, 2017) for different regions and a reasonable

value is used so that the pore pressure prediction matches the geological events in the region. The validity of the *d*-exponent equation depends on an accurate assumption of the estimated NCTL, which is why we used another estimate of pore pressure. Similarly, an expression for PPG (Pore Pressure gradient) can be derived for a riserless hole to estimate the final pore pressure profile (equation 19).

2.2.2 Sonic transit time method

From the relationship between seismic velocity and effective stress, Bowers (1995) postulated that the pore pressure can be estimated from the ratio between effective stress and the velocity in normally pressured sediments. Compressional velocity depends on the grain type, fluid content, and porosity of the different lithologies (Eaton, 1972). The variability of overburden stress gradients (Terzaghi et al., 1968) depends on the region of study but generally are functions of burial depth and pore pressure gradients. Departure of the sonic slowness away from the NCT to higher values indicates evidence of overpressure but true if within the same lithology. Pore pressure gradient can then be estimated considering the shale travel time with the below equation 20.

$$PPG = OBG - (OBG - P_{ng}) \left(\frac{\Delta t_n}{\Delta t} \right)^m \tag{20}$$

Where Δt is transit time in shales from well log, Δt_n is transit time in shales (normal pressure condition), m is an exponent (empirically m is equal to 3). From the geology of the Nankai Trough, it is generally observed that the porosity decreases with depth and lithological change from less compacted to more compacted, decreasing the fluid content and grain size. To estimate the NCTL of shale travel time, we first preprocess the sonic transit time log by filtering and smoothing the data. Then we used equation 21 to generate the normal compaction trend line Δt_n (Fig. 7Ib) by fitting an exponential relationship of sonic travel time relational to the drilled depth.

$$\Delta t_n = \Delta t_m - (\Delta t_{ml} - \Delta t_m)\, e^{-cz} \tag{21}$$

Where Δt_m is transit time in the shale matrix, Δt_{ml} is transit time at the mudline ($Z = 0$), Z is the true vertical depth below mudline (mbsf) and c is the compaction parameter.

3 Results

3.1 DHAP modelling: identification of flowing zones within the borehole

We applied the methodology of section 2.1 to the DHAP data of Hole C0024A. The results are displayed in Fig. 5b, which shows the modeling at various stages: (a) with only the clean water contribution, (b) with all static contributions, i.e. clean water density and cutting weight and (c) with the additional contribution of hydraulic losses associated with mud circulation. The modeling was done for the whole time series, but the vertical profiles only show the times related to actual drilling, when the borehole was extended (Fig. 3, for a description of the time-depth conversion).

3.1.1 Parametric study

In Fig. 5, the fluid injected into the borehole was assumed to be seawater ($\rho_{MW} = 1028$ kg/m^3, $\mu = 1$ mPa $\cdot$ s). This result is quite satisfactory but the mud density used is lower than the one indicated in the daily drilling report with values ($\rho_{MW} = 1350$ kg/m^3, $\mu = 51$ mPa $\cdot$ s). Mixing between the tank mud and seawater could have occurred in the borehole. Hence, we performed a parametric study for the full modeling of the DHAP considering a large range of viscosity and density values for the clean mud, between $1 - 52$ mPa $\cdot$ s and $1028 - 1370$ kg/m^3 respectively (Fig.6). Changing slightly the properties of the clean mud, the model over-predicts the DHAP data significantly. Compared to the reference seawater properties (Fig. 6a), changing slightly either clean mud density (Fig. 6c) or mud viscosity (Fig. 6b), the model overpredicts the baseline of the DHAP data. If the mud properties from the drilling report are applied (Fig. 6d), the model overpredicts the DHAP data by more than $3MPa$.

To quantify the quality of the fit for the whole range of values considered in the parametric studies. We used $L_2 = \frac{1}{z_{decollement}} \int_0^{z_{decollement}} \sqrt{(DHAP(z) - Pred(z))^2} * dz$ to normalized the error for the DHAP prediction above décollement. The L_2 equation is based on the principle of the distance between two points on a 2-dimensional plane. The result (Fig. 6e and f) for slightly varying either density or viscosity properties of the clean mud does not show significant pressure decay. It rather fits within a narrow range with the normalised pressure error close to 0 MPa, while, the mud (drilling report parameters) is completely over predicted with error close to 0.06 MPa.

The effect of slightly varying either the density or viscosity properties of clean mud on the model DHAP is not easily differentiated from this Fig. 6e & f). However, this is already identified on Fig. 6b & c when compared with the clean mud Fig. 6a. The parametric study shows that the model is in good agreement with empirical DHAP data only if the parameters (clean fluid density, viscosity) are close to the seawater data. Therefore, this disputes the mud properties provided by the daily drilling reports that earlier suggested that the mud used for drilling well C00024A is more denser and viscous.

3.1.2 Contribution of cuttings and hydraulic losses on the DHAP

The contribution of rock cuttings to clean mud during drilling (equation 1) is estimated to be between $1.63 - 63$ kg/m^3. This results to a maximum of 6.1% percent rise in the mud effective density value, which ranges from $1029.63 - 1091$ kg/m^3. This suggests that cuttings make a negligible contribution to the clean mud weight. The effective density results back up the assumptions provided in section 2.1.1 for a Eulerian volume system.

The difference between the full static pressure model (with both clean mud and cuttings) and the clean mud model is attributed to the cuttings in Fig. 5b. On Fig. 5b, the static pressure model (clean mud and cuttings) increases slightly above the clean mud pressure, but in a limited fashion. The parametric investigations (Fig. 6b & c) further show that the difference between the static pressure model and clean mud pressure is minor, despite modifying the mud property. The difference remains the same even when the overall mud pressure has increased for the drilling report, as shown in Fig. 6d. Because of its little contribution, the production of cuttings by drilling cannot explain alone the DHAP anomaly of Fig. 2i.

The hydraulic loss along the borehole (equation 8) explains most of the discrepancy between the predicted model and the actual DHAP data (Fig. 5b). It was computed for a turbulent hydrodynamic regime in the annulus of the borehole as suggested by the $Re \gg 50000$ results. Hence, the frictional hydraulic loss was reasonably calculated with the Fanning equation (equation 7). The predicted model fits satisfactorily to the mud pressure (DHAP) data, with a difference less than 1 MPa within the accretionary prism until the décollement zone is reached (Fig. 5c). Then, the pressure anomaly (Fig. 5c) rises to an excess of $2.5 - 5$ MPa at the décollement interval (< 813 mbsf). This mud pressure anomaly entering the décollement was not fully explained by the hydraulic model.

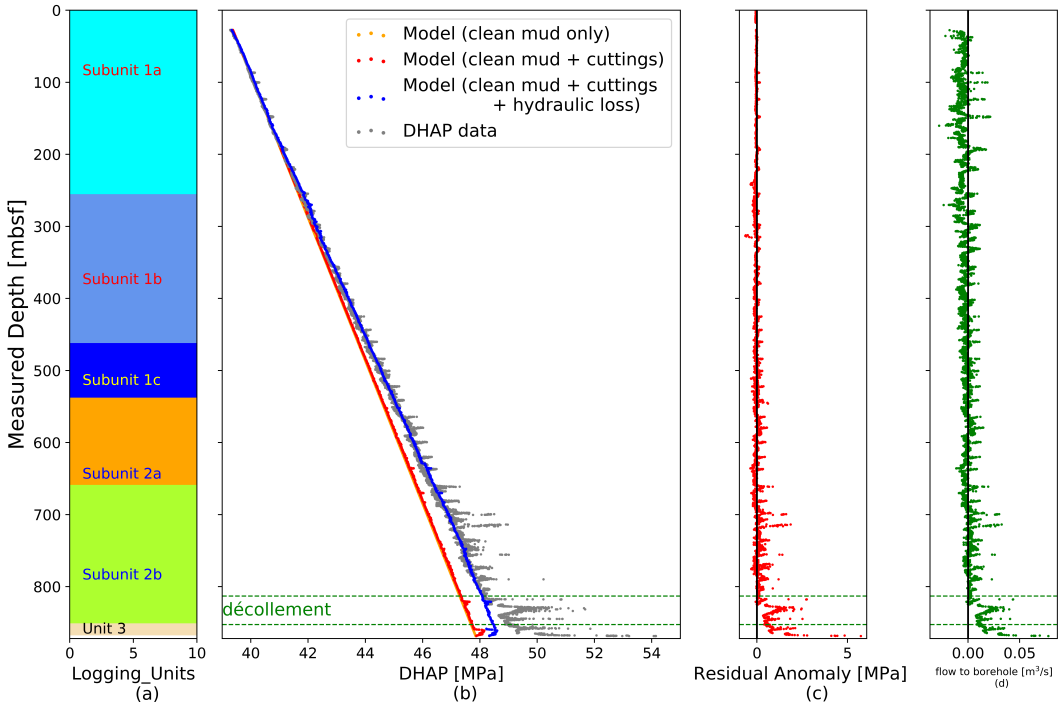

Figure 5. Results derived from the modeling of DHAP data for hole C0024A. (a) Lithological column, same as in Fig. 2a. (b) Predicted profiles of the mud pressure at various stages of the modeling: with only the contribution of the clean injected fluid (orange dots), with the additional contribution of the weight of the cuttings(red dots) and the full model, with hydraulic losses of the flowing mud (blue dots). For all models, the mud is assumed to be seawater ($\rho_{MW} = 1028$ kg/m^3, $\mu = 1$ mPa $\cdot$ s). The DHAP data corresponding to actual drilling times (gray dots) is well fitted by the latter model, except below the 2 décollement zones (dashed green lines). (c) Plot of the difference between the DHAP data (gray dots of in graph (a)) and the prediction from the full DHAP modeling (red dots). The null value, where the model exactly fits the data, is highlighted by a thick vertical line. (d) Flow rate between the formation and the hole. Negative value (to the left of the thick vertical line) corresponds to a flow from the hole to the formation, as expected in normal drilling conditions.

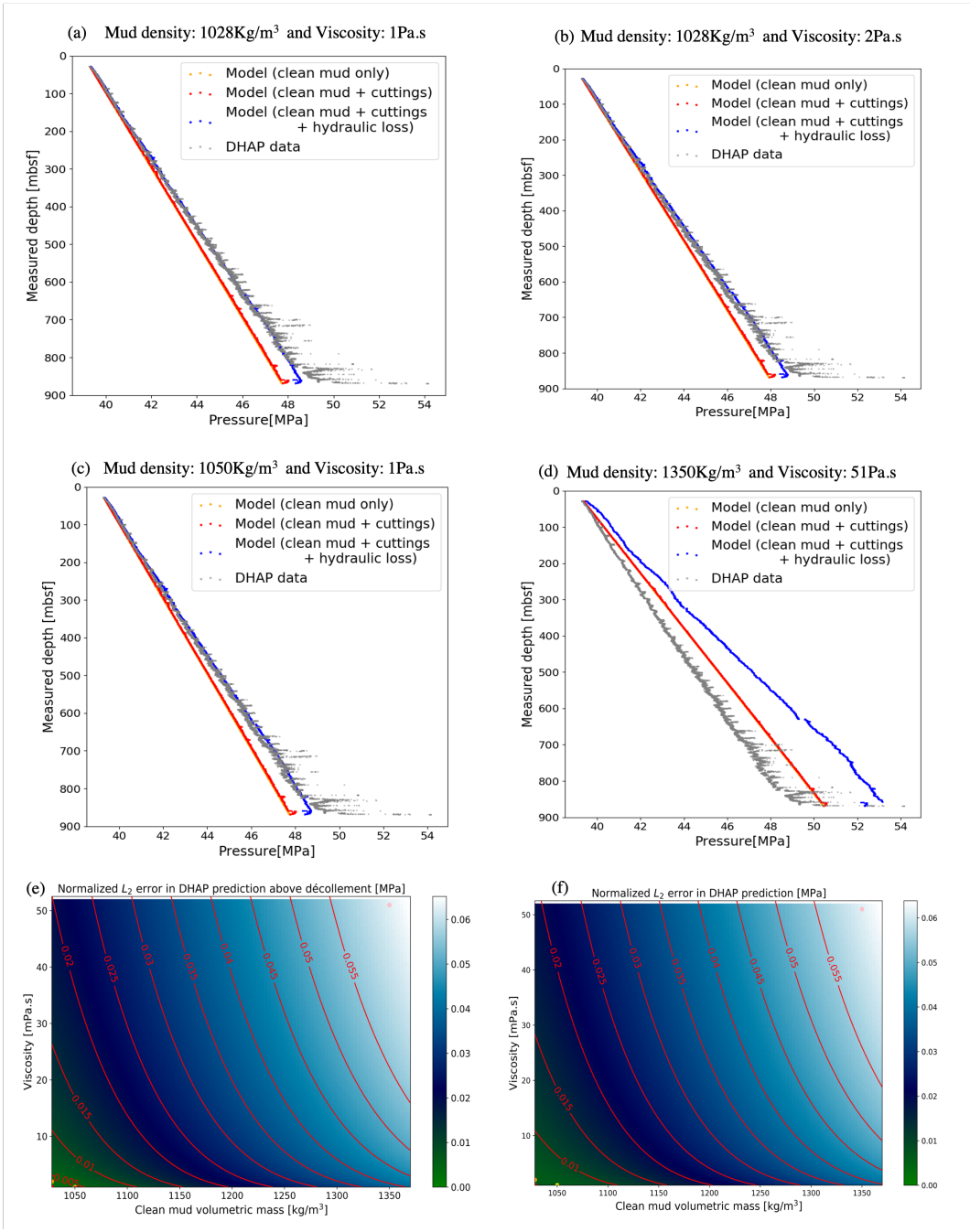

Figure 6. Parametric study of the DHAP modeling for variable mud densities and viscosity values (a) Prediction for a clean mud of density 1028 kg/m^3 and viscosity of 1 Pa · s. (b) Same as (a) but with a slight change in viscosity 2 Pa · s. (c) Same as (a) but with a slight change in density of 1050 kg/m^3 and fixed viscosity 1 Pa · s. (d) Same as (a) with the mud properties wrongly stated in the drilling report with density of 1350 kg/m^3 and viscosity of 51 Pa · s. (e) Normalized L_2 error of the DHAP prediction above décollement, for a range of varying mud properties. Colored dots correspond to the profiles illustrated below: clean mud as water (red), clean mud with varied density (yellow),clean mud with varied viscosity (orange) and drilling report mud properties (pink). (f) Normalized L_2 error for the DHAP prediction for entire borehole length with varying mud properties indicated with coloured dots. The clean mud (red), clean mud with varied density (yellow) and clean mud with varied viscosity (orange) and drilling report mud properties (pink).

Fig. 5d shows the flow between the formation and the borehole. At shallow depths, this flow is negative, meaning mud loss from the borehole to the formation. This is most noticeable between $0 - 462.8$ mbsf (bottom of the logging subunit 1b) and slightly between $627 - 700$ mbsf. Below the 468.8 mbsf, mud loss is zero, indicating that there is no flow exchange between the borehole and formation.

This inflow tames when entering the upper Shikoku basin ($570 - 595$ mbsf & $700 - 770$ mbsf), with a flow rate less than 0.01 m^3/s. This is a zone where the borehole is in gauge (Fig. 8d) and is devoid of fractures (Fig. 8g).

Below décollement, a large amount of fluid flows from the formation into the borehole . The flow rate increases to a maximum of $+0.05$ m^3/s and is most prominent within the two asymmetric damage zones below the two strands of the fault core at a depth of 813 mbsf and 852 mbsf. This large fluid flow (Fig. 5d) into the borehole accounts fully for the significant mud pressure anomaly observed beneath the décollement (Fig. 5c).

3.2 Pore Pressure

The estimated pore pressure profile from the two methods is critically dependent on the construction of a reasonable NCT and its relational variation with the d_{xc} and increase in Δt trend apart from the NCT. Increase in formation pore pressure causes a decrease of d_{xc} and increase of Δt. Therefore,the trend deviations in d_{xc} and Δt relative to the NCT are clear indications of abnormal pressure zones.

The estimated overpressures are denoted as excess pore pressure ($P^* = P_f - P_{hydro}$) above hydrostatic pressures, and the degree to which fluid pressures counteract the total normal stress generated by the lithostatic load is generally stated in the form of an over-pressure ratio $\lambda = \frac{P_f}{P_{litho}}$ and modified excess pore pressure ratio is $\lambda^* = \frac{(P_f - P_{hydro})}{(P_{litho} - P_{hydro})}$. The λ^* value normalizes excess pore pressure relative to the lithostatic pressure (λ^* is 0 at hydrostatic pore pressure and 1 at lithostatic), making it easier to assess the importance of simulated excess pore pressure.

3.2.1 Pore Pressure d_{xc}-exponent

The d_{xc} line does not follow the NCT in Fig. 7b in the depth range of 0-180mbsf (coincides with part of subunit 1a [Fig. 7a]). This interval was not considered when constructing

the NCT, because these facies are assumed to be characterised by unconsolidated sediments from accreted continental or fluid-rich subducting plate sediments still undergoing possible erosional sediment unloading. Hence, it is considered a hydrostatically pressured interval. The d_{xc} line follows the NCT line between 180-490mbsf (comprises part of subunit 1a, 1b & 1c) because it was the primary lithological unit used for constructing the NCT line. The d_{xc} trend is consistent with increasing depth and vertical effective stress. With a pore pressure gradient value of 1.0 g/cm^3 (Fig. A1c) and increasing pressure between 39.37 MPa to 47.8 MPa (Fig. 7c), this depth range is also considered hydrostatically pressured, as illustrated on Fig. 7c & f). Overall, the mud pressure is higher than the pore pressure and hydrostatic pressure between 0-490 mbsf (Fig. 7 f). Hence, the entire interval is considered normally pressured.

In Fig. 7b the d_{xc} begins to depart from the NCT to lower values at the depth of 490 mbsf. This depth coincides within the subunit 1c (Fig. 7a) and it marks the top of the geopressured zone. Therefore, the over-pressured zone is localized between 490 mbsf and the bottom the borehole. The pore pressure variation within this depth range is influenced by the changing d_{xc} value along the trend line. On Fig. 7b, the d_{xc} gradually drops below 1, then gradually increases to a value of 1.06 at a depth of 786.4 mbsf, before decreasing to lower values (0.75) within the décollement interval . The d_{xc} method cannot be rigorously applied below the second strand of the décollement fault core, since the NCT for the footwall sandy lithology is not characterized. But further decrease in the d_{xc} depicts the existence of higher pore pressure.

The pore pressure gradually rises and at the depth of 510.8 mbsf, a crossover between the pore pressure and the DHAP is observed (Fig. 7f). This point marks the onset of higher pore pressure values over the mud pressure and it rises gently to maximum value of 52.6 MPa (Fig. 7f) with localised pore pressure gradient (Fig. A1c) rising up to 1.05-1.6 g/cm^3. This method shows that excess pore pressure ranges $P^* \approx 0.1 - 4.79$ MPa above hydrostatic pressure and the lithostatic load ($\lambda \approx 0.9 - 0.96$, $\lambda^* \approx 0.1 - 0.62$), with the lower range values within the accreted sediments and maximum values below the décollement and the underthrusting sediments. There is localized step in pressure (Fig. 7c & f) when crossing the fault core of the décollement (813 mbsf and 852 mbsf).

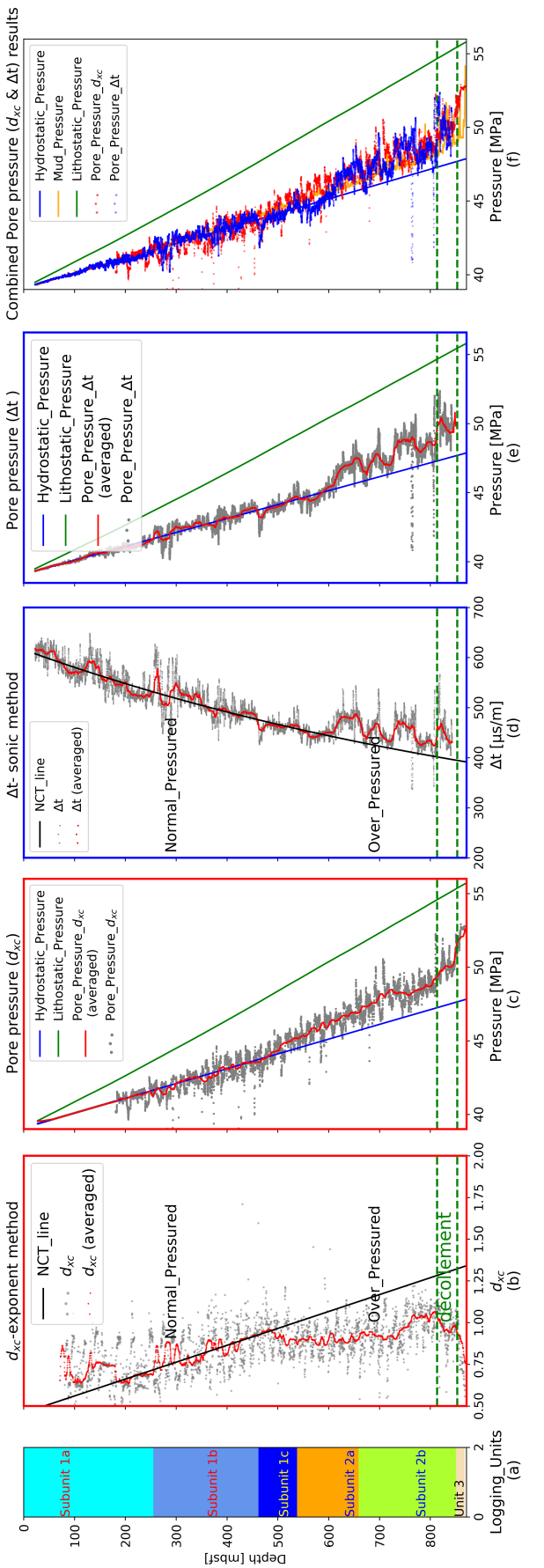

Figure 7. Pore pressure predictions from d_{xc} exponent (the red circled plots [b & c]) and Δt sonic (blue circled plots [d & e]) method. (a) Logging units (b) Profile of the Eaton d_{xc} coefficient (raw d_{xc} [gray] and d_{xc} averaged sampled for 500 points[red]) along the borehole with an observable deviation to lower values from the NCT line (black) at the top of the subunit 1c (accreted wedge Facies). This particular depth marks the top of the geopressured interval. (c) The pore pressure profile (red line) follows hydrostatic pressure (blue line) within the normal pressured zone and rises significantly above the hydrostatic pressure within the overpressured zone. (d) Eaton Δt coefficient profile (raw Δt [gray] and sampled Δt [red]) along the borehole with an observable deviation to higher values from the NCT line (black) within the upper Shikoku facies. (e) The pore pressure profile (red line) follows hydrostatic pressure (blue line) within the normal pressured zone and rises significantly above the hydrostatic pressure within the overpressured zone. (f) Overlay comparing both pore pressure results from the Eaton's methods. The two pressure profiles (d_{xc} in red and Δt in blue) almost overlap close to the décollement with a localised increase in pore pressure across the strands. For the two methods, the pore pressure profile follows hydrostatic pressure (blue line) and less than the mud pressure within the normal pressure zone. While within the overpressured zone, the pore pressure rises above the mud pressure and hydrostatic pressure down to the bottom of the borehole.

3.2.2 Pore pressure determined from sonic transit time

The sonic transit time follows the NCT (Fig. 7d) between the depth range of 0 to 580 mbsf. It coincides with the Unit 1 (accretionary trench wedge facies) and the top part of the subunit 2a (upper part of Shikoku basin hemipelagic-pyroclastic facies) (Fig. 7a). With a pore pressure gradient value of 1.0 g/cm^3 (Fig. A2c) and increasing pressure between 39.37 MPa to 47.8 MPa (Fig. 7e), this depth range is also considered hydrostatically pressured, as illustrated on Fig. 7e). Overall, the mud pressure is above pore pressure (Fig. 7f) and the hydrostatic pressure between 0-580 mbsf. Hence, this interval is considered normally pressured.

The Δt line departs significantly from the NCT to higher increasing slowness of transit time in this lithologies at a depth of 580 mbsf (Fig. 7e). The depth coincides with the upper part of Shikoku basin hemipelagic-pyroclastic facies (Fig. 7a) and it marks the top of the geopressurized zone. Therefore, the over-pressured zone is defined as the depth range between 580 mbsf and 871 mbsf (bottom of the borehole). The pore pressure gradually rises and at the depth of 611 mbsf, a crossover between the pore pressure and the DHAP is observed on Fig. 7f. This point marks the onset of higher pore pressure values over the mud pressure and it rises gently to maximum value of 50.83 MPa (Fig. 7f) with localised pore pressure gradient (Fig. A2c) rising up to 1.06-1.4 g/cm^3.

This method shows that excess pore pressure ranges $P^* \approx 0.05$–3.03 MPa above hydrostatic pressure and the lithostatic load ($\lambda \approx 0.89 - 0.92$, $\lambda^* \approx 0.1 - 0.41$), with the lower range values within the accreted sediments and maximum values below the décollement and the underthrusting sediments. There is localized step in pressure (Fig. 7e & f) when crossing the fault core of the décollement (813 mbsf) into the first asymmetric damage zones of the footwall as observed using the d-exponent method (Fig. 7e).

4 Discussion

4.1 Reliability of flow modeling and pore pressure prediction

Two independent methods were applied to the C0024A dataset. First, fluid flow modeling from the mud pressure shows that more fluid comes from the formation into the borehole at greater depths. Secondly, Eaton's equations predict an increase in pore pressure with depth. Unfortunately, no other hydraulic data were obtained from the C0024A well dataset, like pumping tests, long-term observatories, and cores. To compensate, (1) self-consistency

of behavior of the flow profile and the pore pressure profiles are examined and (2) the consistency of the hydraulic predictions are checked against other independent proxies.

First, both pore pressures determined from the Eaton's method converge (Fig. 7). Within the limit of resolution of the methods (about 2MPa, as seen from the scatter of the pressure determined from the raw data), they both overlay and highlight two features: (1) below 600 mbsf, the pore pressure departs from the hydrostatics and (2) the pore pressure increases again when crossing the first strand of the décollement. Given the sonic data were not acquired on the second strand, only d_{xc} prediction suggests another step in pressure on this strand.

Secondly, we compare the DHAP modeling. Given some possible packoffs (transient blocking of the annulus by rocks collapsing from the borehole wall along the drillstring), that can introduce transient peaks in the mud pressure and hence in the inflow computation, the interpretation will be based on the long-term baseline of the flow prediction of Fig. 8i.

DHAP analysis shows that mud pressure is lost to the formation (Fig. 8i & Fig. 5d) within the logging subunit 1a (unconsolidated sediments possibly still undergoing reactivation) and subunit 1b. This loss is consistent with the predictions by Eaton's method that show that mud pressure is higher than the formation pore pressure (Fig. 8j). This is typical of a safe drilling procedure.

The loss of mud pressure to the formation becomes null around 462.8 mbsf. Consistently, at the same depth, the pore pressure rises and becomes equal to the mud pressure. The flow shifts to the right (positive) side of the baseline (Fig. 8i) when the pressure predictions from both Eaton methods converge to a value higher than the mud pressure, around 615 mbsf. This provides a self-consistent picture of the flow.

When the mud pressure exceeds the pore pressure, the borehole becomes unstable (Fig. 8d), as seen by the more infrequent peaks in the mud pressure time series during non-drilling periods, that is attributed to packoffs. This higher pore pressure in the hemipelagites also explains the difficulties met when coring the C0024F borehole, which could go beyond 731 mbsf (Tobin et al., 2020).

Other geophysical proxies are consistent with a rise in pore pressure below 490 mbsf. The ratio V_P/V_S decreases from that depth (Fig. 8k) suggesting also higher pore pressure. The borehole images (Fig. 8b) also show a change in the breakout direction from that depth,

consistent with a change in effective stress that could be related to a non-hydrostatic pore pressure.

The large flow predicted at the base of the borehole is consistent with the sharp increase in real-time mud temperature at the base of the hole (Fig. 8l). This is consistent with hot fluids from the formation heating the cold borehole mud injected from the surface.

4.2 Pore pressure increase in the accretionary prism

The Eaton's method shows that the distribution of increased pore pressures in the Nankai subduction zone are not only restricted within the fault zones but also pervasive within the accretionary prism.

Both Eaton's methods converge to an excess of pore pressure in the hemipelagites, suggesting a departure from normal compaction. Either this anomaly existed prior to subduction, or this anomaly is related to the accretion process.

IODP Expedition 322 of the NanTroSEIZE project was dedicated to the characterization of the subduction inputs, by sampling the sedimentary column entering the accretionary prism in sites C0011 and C0012. From these samples, Hüpers et al. (2015) show zone of anomalously high porosity in the subduction input. This anomaly was explained by the inclusion of volcanic ashes in the sediment, whose silica strengthened the skeleton and prevents further compaction. The volcanic ashes can be identified as highs in gamma-ray logs Hüpers et al. (2015).

In C0024A, Tobin et al. (2020) identify this anomalous high porosity zone from subduction inputs as a change in porosity at 550 mbsf from electrical logs and from the MAD (Moisture and density) study from the cores of hole COO24E and related to this zone. This high porosity could affect the sonic log and alter the pore pressure estimation while using Eaton method. This high porosity should also be associated with an increase in permeability and hence with an increase in flow from the borehole to the formation if there were no hydraulic anomalies.

On the contrary, our analysis of DHAP data shows diminishing flow, and even inflow from the formation below 700 mbsf, which requires the pore pressure to be larger than the mud pressure. Moreover, the high porosity zone is limited in the upper layer of the Shikoku hemipelagics, being 150 m thick in C0011 hole, whereas we show that the pore pressure

tends to increase steadily with depth over the whole layer of Shikoku hemipelagic clay, even in the zones of low gamma-ray.

To summarize, the hydraulic anomaly cannot be discarded as an artefact caused by the porosity anomaly within the sedimentary column entering the subduction. Whereas this initial anomaly affects the occurrence of the anomaly, it cannot explain alone the high pressure in the hanging wall.

The accretion of the layers to the prism introduces additional compressional lateral stress onto these formations. In addition, the seismic cross-section of Fig. 1b shows that the slope of the prism evolves with time: a splay fault causes the overthrusting of the landwards sediments onto the layers on which Hole C0024A is drilled, and the deposition of slope sediment on its footwall. Our pore pressure prediction provides an additional constraint for the modeling and understanding of these processes.

According to the seismic cross-section of Fig. 1, Hole C0024A intersects faults at 171 mbsf, 281 mbsf and 441 mbsf. Since transient peaks in flow rate are not considered in our interpretation, local flow along these faults could not be identified. Crossing these faults does not introduce any large-scale change in pressure, contrary to the décollement. Given that these faults were not identified on the borehole image ((Tobin et al., 2020) and Fig. 8g), these faults can be considered as minor, without significant hydraulic influence.

In general, our findings demonstrate that within the frontal thrust 3 km from the trench, the maximum excess pore pressure is $P^* = 0.04 - 4.79$ MPa and lithostatic load ($\lambda = 0.88 - 0.96$ & $\lambda^* = 0.1 - 0.62$) below décollement and it is further expected that 20km or more away from the trench towards the locked seismogenic zone the excess pore pressure should increase above 5-20 MPa (Tobin & Saffer, 2009). Our findings are consistent with core & borehole-based studies by Saffer (2003), E. J. Screaton et al. (2002) that even within $\sim$1–4 km of the trench, pore pressure of underthrusting sediments is typically more than 60–70% of the lithostatic load ($\lambda = 0.68$–0.97; λ^*=0.20–0.91).

Using data from IODP drilling sites 808 and 1174, (Flemings & Saffer, 2018; Zhang et al., 2021) found that the Nankai's underthrust sequence is overpressured, with P^* range 3.4 to 4.2 MPa and λ^* range 0.7 to 0.9 based on experimental and numerical modeling. However, the IODP drill sites 808 and 1174 are about 185 kilometers south-west of the well

C0024A used in these research, explaining the slight difference with the overpressurization state presented here.

4.3 Hydraulic structure of the décollement zone

Fig. 9 focus on the décollement and compile our new hydraulic information together with preexisting information, interpreted by Tobin et al. (2020). The décollement zone is associated with a fluid flow anomaly zone, with indications of fluid exchange from the formation into the borehole (Fig. 9h). The décollement is complex, with two strands at 813 mbsf and 851 mbsf. Each strand is asymmetric, with a fault core near the hanging wall and damage zones a few meters thick ($6 - 8$m) concentrated in the footwall.

Although no core could be retrieved in the décollement, the zone was investigated through a full suite of geophysical logs (Fig. 9). The asymmetric damage zones are characterised as conductive zones as seen on the electrical borehole imaging from deep resistivity (Fig. 9b), mechanically weak zones as indicated by the larger borehole diameter (Fig. 9c), a steady low P-wave velocity interval (Fig. 9d), a low deep resistivity (Fig. 9e). The fault core was identified as a sharp decrease in resistivity (Fig. 9e) and a larger caliper (Fig. 9c).

The new hydraulic information is shown within the blue frames of Fig. 9. Each strand is associated with an increase in pore pressure (9i), but the increase in flow is more localised (Fig. 9h), and related to large-scale fractures visible on the image logs (Fig. 9b & f) at 813mbsf and 852mbsf. After this last fracture, the flow rate keeps large values. The permeability of the damage zone is therefore fracture-supported and not matrix-supported.

The fault core marks the top of the mechanically weak damage zones (Fig. 9c), both the model DHAP and the original DHAP data are flat with no peaks (Fig. 9g), and marked with a step in pore pressure (Fig. 9i). It is directly overlain by a hemipelagites hanging wall (Fig. 8c) with lithological characteristics comparable to those of a normal cap/seal lithology, suggesting that the fine-grained sediments may smear along the fault plane during fault movement, contributing to the fault core's sealing capacity. Hence, the fault core is considered as impermeable and hydraulic seal.

Our findings are consistent with the hypothesis that the impermeable décollement acts as a barrier to upward fluid convection (Gamage & Screaton, 2006; Saffer & Tobin, 2011),

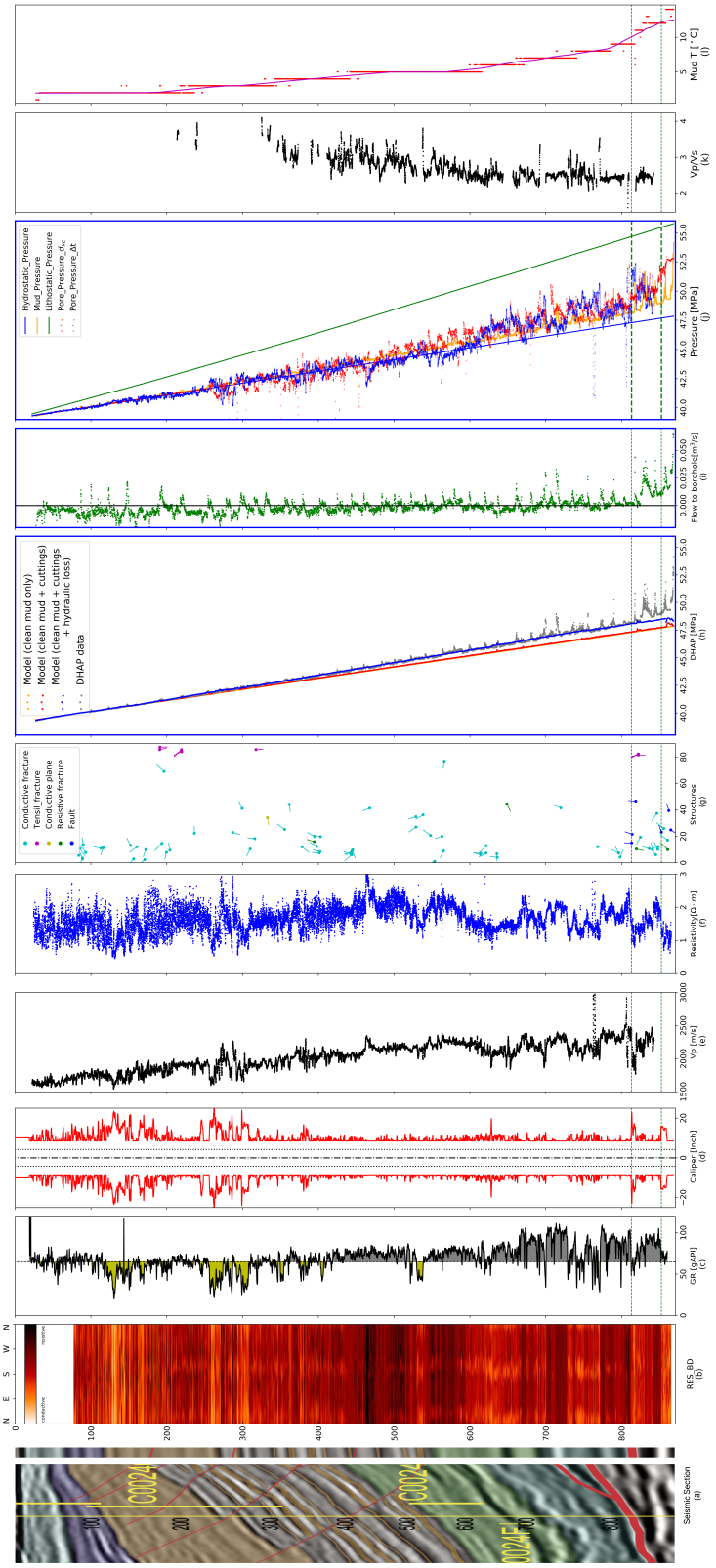

Figure 8. Summary of the hydraulic properties determined along the whole Hole C0024A. (a) seismic section (b) Electrical borehole imaging from deep resistivity (c) Gamma-ray (d) caliper log (e) P-wave velocity (f) deep resistivity (g) tadpoles of the major structures picked on the electrical image (h) raw DHAP data, modeled DHAP, effective mud density and tank mud density (i) Fluid flow exchange between the formation and the borehole (j) Pore pressure estimated from the 2 Eaton methods, hydrostatic and overburden pressure (k) ratio of P-wave velocity and shear velocity (l) mud fluid temperature.

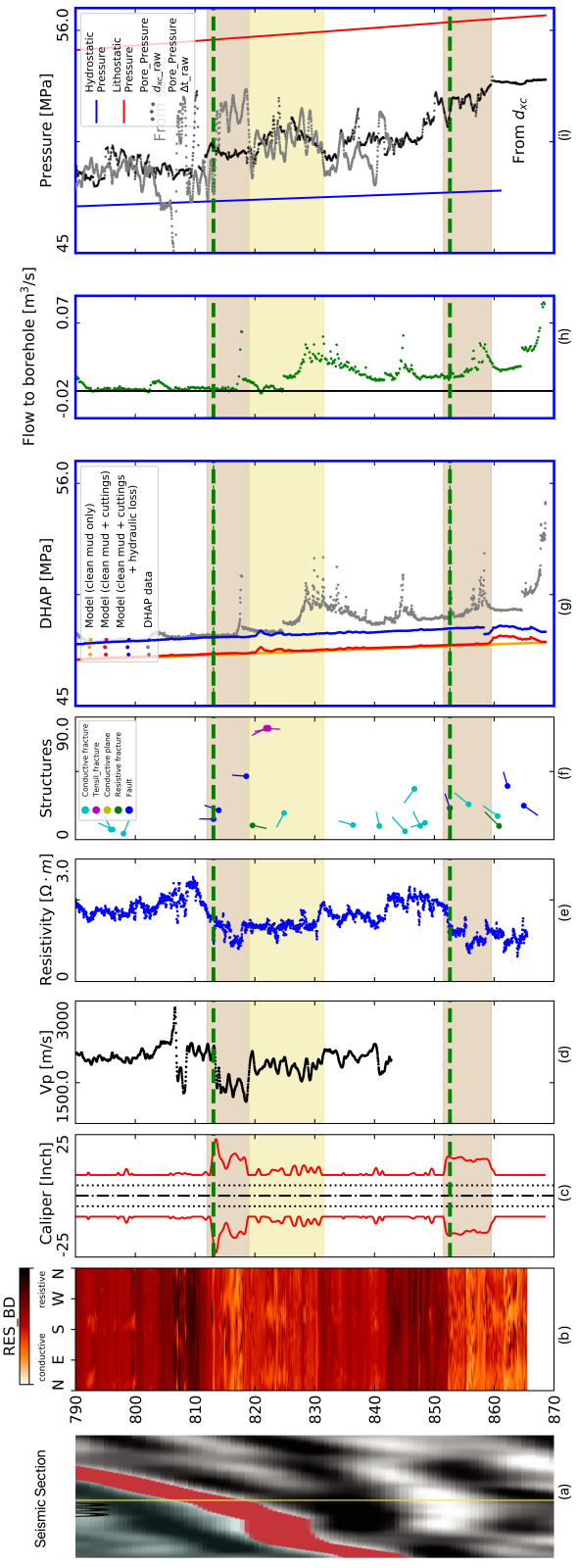

Figure 9. [1] Summary of the hydraulic properties determined along Hole C0024A, with focus on the décollement zone, below 780 mbsf. (a) Seismic section (b) Electrical borehole imaging from deep resistivity (c) caliper log (d) P-wave velocity, (e) deep resistivity, (f) tadpole diagram of the major structures picked on the electrical image (g) raw DHAP data, modeled DHAP, effective mud density and tank mud density (h) Fluid flow exchange between the formation and the borehole (i) Pore pressure estimated from the 2 Eaton methods, hydrostatic and overburden pressure.

meaning that there is no hydrologic connection between accreted and underthrust sediments below the décollement (i.e they are made up of different hydrogeological systems).

The study here examines only the toe of the accretionary prism; the hydrological status may be different in other locations. For example, Zhang et al. (2021) discovered that in site 1173, west of the Nankai Trough, both accreted and underthrust sediments form a single hydrogeological system and that the décollement does not act as a fluid barrier. Our findings are novel since they are based entirely on data from LWD and MWD tools, which provide high resolution *in situ* information about the characteristics of various lithologies along the borehole length.

4.4 Implication of high pore pressure on seismotectonics

Numerous influences on the spatial and temporal distribution of slips have been hypothesized. Physical features of the fault zone, as well as variations in the distribution and composition of pore fluids and pore pressure, are critical (Kitajima & Saffer, 2012; Song et al., 2009; Warren-Smith et al., 2019; Liu & Rice, 2007). Our research provides more insights into how faults, pore fluid pressure, and fluid flow interact.

As previously noted, our findings indicate that significant pore fluid pressure exists below the décollement. This rise in fluid pressure affects the reduction of the effective stress state acting on the fault zone (Rubey & King Hubbert, 1959). Due to delayed consolidation or hydrofracture and dilatation within the fault zone, a rise in fluid pressure results in decreases in effective stress, V_p, and acoustic impedance reversal across the fault (J. Moore et al., 1995).

It is inferred in this study that when sediments travel deep into the subduction zone, the pore fluid pressure will be large, which could explain the high frequency of Low Frequency Earthquakes (LFE), the drop in sonic anomaly, and the decrease in effective stress, all of which contribute to this zone being mechanically weak and predominately aseismic plate boundary (Kitajima & Saffer, 2012).

A further inference here is that since well C0006 data suggests that the toe of the accretionary prism is full of permeable sandy sediments (J. C. Moore et al., 2013). The connection of the toe should be a drainage of the higher pressure pocket. Thus, the pore pressure is primarily derived from deeper depths known as low velocity zones (Park et al.,

2010), and these transient pulses may be related to the SSE in the Nankai subduction zone and could be the initiation of large tsunamigenic earthquakes in this trough.

5 Conclusion

In this manuscript, we developed a methodology to characterize the hydraulic state along the C0024A borehole, by processing both drilling and geophysical data, in both time and space. The results provide a self-consistent description of the fluid flow and pore pressure profile along the hole. This shows that high pore pressure is pervasive within the accretionary prism and not only restricted only to the fault zone. The décollement fault zone is associated with a hydraulic anomaly with large fluid flow in excess of 0.05 m^3/s and high pore pressure to excess of $P^* = 0.04 - 4.79$ MPa and lithostatic load ($\lambda = 0.88 - 0.96$& $\lambda^* = 0.1 - 0.62$) and coupled with higher permeability.

Our consistent results have further shown that the toe of the accretionary prism is characterised by high pore pressure, hence it will favour the occurrence of SSE and tsunamigenic earthquakes. This study helps characterizing the hydromechanical state of a plate boundary and refining the potential of the décollement to be the locus of devastating tsunamigenic earthquakes. This study is a first step to understand the full hydraulics of the Nankai subduction zone, since several other holes were drilled during the NanTroSEIZE campaigns, with similar time series of LWD annulus pore pressure data, hence the methodology can be replicated.

Acknowledgments

Special appreciation to the staff onboard Chikyu drilling vessel for their expertise and their kindness. MLD also thank David Castillo for discussion on the processing of drilling data, both in time and space. We appreciate the Petroleum Technology Development Fund (PTDF) Nigeria, for funding the PhD research.

References

Amiri, H., & Doan, M.-L. (2019). Hydrological features across the Japan Trench , derived from pressure while drilling of expedition IODP 343 (J-FAST). In *American Geophysical Union, Fall Meeting* (pp. T51G–0377).

Araki, E., Saffer, D. M., Kopf, A. J., Wallace, L. M., Kimura, T., Machida, Y., ... Davis, E. (2017). Recurring and triggered slow-slip events near the trench at the Nankai

Trough subduction megathrust. *Science*, *356*(6343), 1157–1160. doi: 10.1126/science.aan3120

Audet, P., Bostock, M. G., Christensen, N. I., & Peacock, S. M. (2009). Seismic evidence for overpressured subducted oceanic crust and megathrust fault sealing. *Nature*, *457*(7225), 76–78. doi: 10.1038/nature07650

Bingham, M. G. (1965). *A new approach to interpreting rock drillability.* Petroleum Pub. Co.

Blasius, H. (1913). *Das Ähnlichkeitsgesetz bei Reibungsvorgängen in Flüssigkeiten.* Berlin Heidelberg: Springer.

Bourgoyne, A. T., Millheim, K. K., Chenevert, M. E., & Young, F. S. (1986). *Applied Drilling Engineering.* Society of Petroleum Engineers.

Boutt, D. F., Saffer, D. M., Doan, M., Lin, W., Ito, T., Kano, Y., ... Moe, K. T. (2012). Scale dependence of in-situ permeability measurements in the nankai accretionary prism: The role of fractures. *Geophysical Research Letters*, *39*(7). doi: 10.1029/2012GL051216

Bowers, G. (1995). Pore pressure estimation from velocity data : Accounting for overpressure mechanisms besides undercompaction. *Society of petroleum engineers*, *SPE 27488*(June), 89–95.

Dewan, J. T., & Chenevert, M. E. (2001). A model for filtration of water-base mud during drilling: Determination of mudcake parameters. *Petrophysics*, *42*(3), 237–250.

Eaton, B. A. (1972). The effect of overburden stress on geopressure prediction from well logs. *Journal of Petroleum Technology*, *24*(08), 929–934. doi: 10.2118/3719-pa

Eaton, B. A. (1975). *The equation for geopressure prediction from well logs.* (SPE-5544-MS) doi: 10.2118/5544-MS

Flemings, P. B., & Saffer, D. M. (2018). Pressure and Stress Prediction in the Nankai Accretionary Prism: A Critical State Soil Mechanics Porosity-Based Approach. *Journal of Geophysical Research: Solid Earth*, *123*(2), 1089–1115. doi: 10.1002/2017JB015025

Gamage, K., & Screaton, E. (2006). Characterization of excess pore pressures at the toe of the Nankai accretionary complex, Ocean Drilling Program sites 1173, 1174, and 808: Results of one-dimensional modeling. *Journal of Geophysical Research: Solid Earth*, *111*(4), 1–13. doi: 10.1029/2004JB003572

Hüpers, A., Ikari, M. J., Dugan, B., Underwood, M. B., & Kopf, A. J. (2015). Origin of a zone of anomalously high porosity in the subduction inputs to Nankai Trough. *Marine*

Geology, *361*, 147–162. doi: 10.1016/j.margeo.2015.01.004

Jorden, J. R., & Shirley, O. J. (1966). Application of drilling performance data to overpressure detection. *Journal of Petroleum Technology*(49), 1387–1394. doi: 10.2118/1407-pa

Kitajima, H., & Saffer, D. M. (2012). Elevated pore pressure and anomalously low stress in regions of low frequency earthquakes along the Nankai Trough subduction megathrust. *Geophysical Research Letters*, *39*(23), 1–5. doi: 10.1029/2012GL053793

Kodaira, S., Iidaka, T., Kato, A., Park, J. O., Iwasaki, T., & Kaneda, Y. (2004). High pore fluid pressure may cause silent slip in the Nankai Trough. *Science*, *304*(5675), 1295–1298. doi: 10.1126/science.1096535

Liu, Y., & Rice, J. R. (2007). Spontaneous and triggered aseismic deformation transients in a subduction fault model. *Journal of Geophysical Research: Solid Earth*, *112*(9), 1–23. doi: 10.1029/2007JB004930

Miller, S. A. (2013). The Role of Fluids in Tectonic and Earthquake Processes. In *Advances in geophysics* (Vol. 54, pp. 1–46). Elsevier Inc. doi: 10.1016/B978-0-12-380940-7.00001-9

Moore, J., Moran, K., MacKay, M., & Tobin, H. (1995). Frontal Thrust, Oregon Accretionary Prism: Geometry, Physical Properties, and Fluid Pressure. *Proceedings of the Ocean Drilling Program, 146 Part 1 Scientific Results*(December). doi: 10.2973/odp.proc.sr.146-1.224.1995

Moore, J. C., Barrett, M., & Moe, K. T. (2013). Fluid pressures and fluid flows from boreholes spanning the NanTroSEIZE transect through the Nankai Trough, SW Japan. *Tectonophysics*, *600*, 108–115. doi: 10.1016/j.tecto.2013.01.026

Obara, K., & Ito, Y. (2005). Very low frequency earthquakes excited by the 2004 off Kii peninsula earthquakes: A dynamic deformation process in the large accretionary prism. *Earth, Planets and Space*, *57*(4), 321–326. doi: 10.1186/BF03352570

Park, J. O., Fujie, G., Wijerathne, L., Hori, T., Kodaira, S., Fukao, Y., ... Taira, A. (2010). A low-velocity zone with weak reflectivity along the Nankai subduction zone. *Geology*, *38*(3), 283–286. doi: 10.1130/G30205.1

Rehm, B., & McClendon, R. (1971). *Measurement of formation pressure from drilling data.* (SPE-3601-MS) doi: 10.2118/3601-MS

Rubey, W. W., & King Hubbert, M. (1959). Role of fluid pressure in mechanics of overthrust faulting: II. Overthrust belt in geosynclinal area of western Wyoming in light of fluid-

pressure hypothesis. *Bulletin of the Geological Society of America*, *70*(2), 167–206. doi: 10.1130/0016-7606(1959)70[167:ROFPIM]2.0.CO;2

Saffer, D. M. (2003). Pore pressure development and progressive dewatering in underthrust sediments at the Costa Rican subduction margin: Comparison with northern Barbados and Nankai. *Journal of Geophysical Research: Solid Earth*, *108*(B5), 1–16. doi: 10.1029/2002jb001787

Saffer, D. M., Flemings, P. B., Boutt, D. F., Doan, M., Ito, T., McNeill, L. C., ... Toczko, S. (2013). In situ stress and pore pressure in the kumano forearc basin, offshore SW Honshu from downhole measurements during riser drilling. *Geochemistry, Geophysics, Geosystems*, *14*(5), 1454–1470. doi: 10.1002/ggge.20051

Saffer, D. M., & Tobin, H. J. (2011). Hydrogeology and Mechanics of Subduction Zone Forearcs: Fluid Flow and Pore Pressure. *Annual Review of Earth and Planetary Sciences*, *39*(1), 157–186. doi: 10.1146/annurev-earth-040610-133408

Screaton, E. (2006). Excess pore pressures within subducting sediments: Does the proportion of accreted versus subducted sediments matter? *Geophysical Research Letters*, *33*(10), 17–20. doi: 10.1029/2006GL025737

Screaton, E., & Ge, S. (1997). An assessment of along-strike fluid and heat transport within the Barbados Ridge accretionary complex: Results of preliminary modeling. *Geophysical Research Letters*, *24*(23), 3085–3088. doi: 10.1029/97GL03097

Screaton, E. J., & Saffer, D. M. (2005). Fluid expulsion and overpressure development during initial subduction at the Costa Rica convergent margin. *Earth and Planetary Science Letters*, *233*(3-4), 361–374. doi: 10.1016/j.epsl.2005.02.017

Screaton, E. J., Saffer, D. M., Henry, P., & Hunze, S. (2002). Porosity loss within the underthrust sediments of the Nankai accretionary complex: Implications for overpressures. *Geology*, *30*(1), 19–22. doi: 10.1130/0091-7613(2002)030⟨0019:PLWTUS⟩2.0.CO;2

Song, T. R. A., Helmberger, D. V., Brudzinski, M. R., Clayton, R. W., Davis, P., Pérez-Campos, X., & Singh, S. K. (2009). Subducting slab ultra-slow velocity layer coincident with silent earthquakes in Southern Mexico. *Science*, *324*(5926), 502–506. doi: 10.1126/science.1167595

Spinelli, G. A., & Wang, K. (2008). Effects of fluid circulation in subducting crust on Nankai margin seismogenic zone temperatures. *Geology*, *36*(11), 887–890. doi: 10.1130/G25145A.1

Terzaghi, K., Peck, R. B., & Mesri, G. (1968). *Soil Mechanics in Engineering Practice* (3rd

ed.). Wiley.

Thu, M. K., Ito, T., Lin, W., Doan, M., Boutt, D. F., Kawamura, Y., ... Tobin, H. J. (2012). Operational review of the first wireline in situ stress test in scientific ocean drilling. *Scientific Drilling*(13), 35–39. doi: 10.2204/iodp.sd.13.06.2011

Tobin, H., Hirose, T., Ikari, M., Kanagawa, K., Kimura, G., Kinoshita, M., ... Saito, S. (2020, July). Expedition 358 summary. In *Volume 358: NanTroSEIZE plate boundary deep riser 4: Nankai seismogenic/slow slip megathrust.* International Ocean Discovery Program. doi: 10.14379/iodp.proc.358.101.2020

Tobin, H., & Saffer, D. (2009). Elevated fluid pressure and extreme mechanical weakness of a plate boundary thrust, Nankai Trough subduction zone. *Geology*, *37*(8), 679–682. doi: 10.1130/G25752A.1

Warren-Smith, E., Fry, B., Wallace, L., Chon, E., Henrys, S., Sheehan, A., ... Lebedev, S. (2019). Episodic stress and fluid pressure cycling in subducting oceanic crust during slow slip. *Nature Geoscience*, *12*(6), 475–481. doi: 10.1038/s41561-019-0367-x

Zhang, J., Hüpers, A., Kreiter, S., & Kopf, A. J. (2021). Pore Pressure Regime and Fluid Flow Processes in the Shallow Nankai Trough Subduction Zone Based on Experimental and Modeling Results from IODP Site C0023. *Journal of Geophysical Research: Solid Earth*, *126*(2), 1–19. doi: 10.1029/2020JB020248

Zhang, J., & Yin, S. (2017). Real-time pore pressure detection: Indicators and improved methods. *Geofluids*(1). doi: 10.1155/2017/3179617

Appendix A Supplementary figures

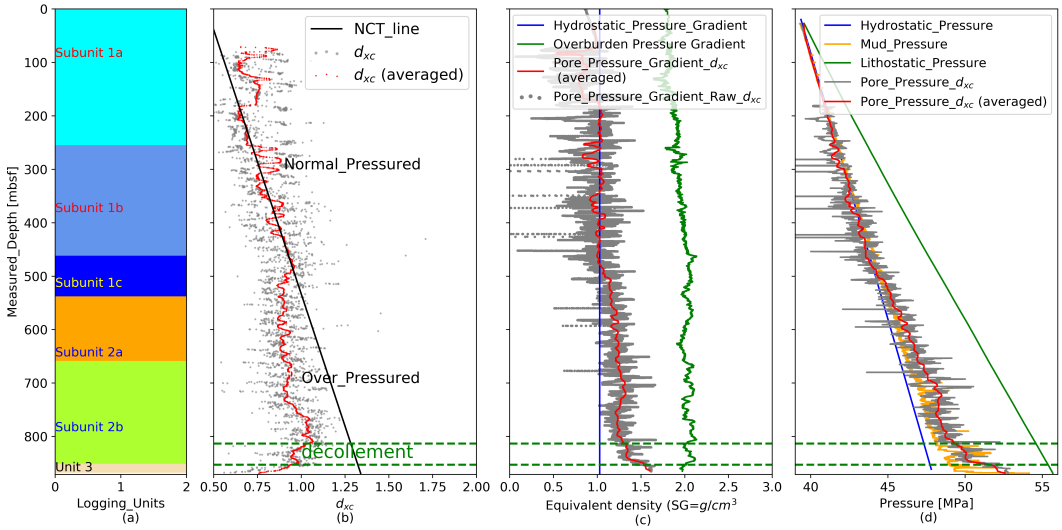

Figure A1. Pore pressure prediction from $d-$exponent method. (a) Logging units. (b) Profile of the Eaton d_{xc} coefficient (raw d_{xc} [gray] and sampled d_{xc} [red]) along the borehole with an observable deviation to lower values from the NCT line (black) at the top of the subunit 1c (accreted wedge Facies). This particular depth marks the top of the geopressured interval. (c) The plot of the variable pressure gradients, the hydrostatic pressure gradient in blue coloured line, overburden or lithostatic pressure gradient in green coloured line, averaged pore pressure gradient in red line, raw pore pressure gradient in gray line. (d) The pore pressure profile follows hydrostatic pressure (blue line) and less than the mud pressure (orange line) within normal pressure zone. While within the overpressured zone the pore pressure rises above the mud pressure and hydrostatic pressure to the bottom of the borehole.

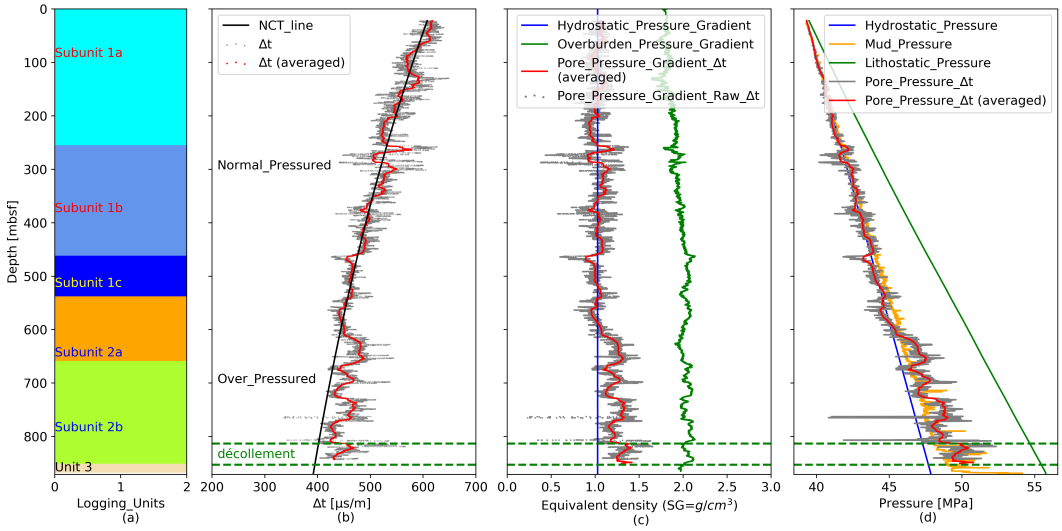

Figure A2. Pore pressure prediction from Eaton modeling based on Δt sonic method (a) Logging units (b) Eaton Δt coefficient profile (raw Δt [gray] and average sampled Δt [red]) along the borehole with an observable deviation to higher values from the NCT line (black) within the upper Shikoku facies. (c) The plot of the variable pressure gradients, the hydrostatic pressure gradient in blue coloured line, overburden or lithostatic pressure gradient in green coloured line, averaged sampled pore pressure gradient in red line, raw pore pressure gradient in gray coloured line. (d) The pore pressure profile follows hydrostatic pressure (blue line) and less than the mud pressure (orange line) within normal pressure zone. While within the overpressured zone the pore pressure rises above the mud pressure and hydrostatic pressure to the bottom of the borehole.